SECOND-ORDER CREST STATISTICS OF REALISTIC SEA STATES

MARIOS CHRISTOU
Shell International Exploration and Production, 2288 GS Rijswijk, The Netherlands.
E-mail: marios.christou@shell.com

PETER TROMANS
Ocean Wave Engineering Ltd., 5 Pine Walk, Liss, United Kingdom.
E-mail: pt7185@hotmail.com

LUC VANDERSCHUREN
Engineering Systems, Avenue Molire, 5/5, 1300 Wavre, Belgium.
E-mail: Luc.vanderschuren@skynet.be

KEVIN EWANS
Shell International Exploration and Production, 2288 GS Rijswijk, The Netherlands.
E-mail: kevin.ewans@shell.com

1. INTRODUCTION

Current engineering design employs second-order irregular wave theory to predict extreme crest elevations (Forristall, 2000). However, there are several field measurements of waves with crest elevations significantly larger than those predicted at second-order; the New Year Wave at the Draupner East platform being one such example (Haver and Anderson, 2000). Consequently, several authors have sought explanations for the occurrence of these so-called *freak*, *rogue* or *abnormal* waves. These explanations include crossing-seas (Donelan and Magnusson, 2005) and higher-order unidirectional effects (Baldock et al., 1996; Gibson and Swan, 2007).

Considering the second-order distribution (Forristall, 2000), there are two distinct shortcomings. First, the crest statistics are based on second-order, time-domain simulations that employ the JONSWAP spectrum and therefore are only strictly applicable for unimodal JONSWAP spectra. Evidence of this is given by Bitner-Gregersen and Hagen (2003) who have found discrepancies between Forristall's distribution in bimodal sea states. Second, it neglects nonlinear effects that occur beyond second-order. These higher-order effects have been demonstrated by (Gibson and Swan, 2007) who found local and rapid energy shifts occurring in the vicinity of an extreme event on account of third-order resonant interactions. These energy shifts are dependent on both the frequency bandwidth and the directional spreading of the underlying spectrum.

The first shortcoming can be overcome by employing the Spectral Response Surface (SRS) method (Tromans and Vanderschuren, 2004), which has no restriction on spectral shape and has been applied to combined wind-sea and swell sea states by Tromans et al. (2007). The second shortcoming has been resolved by Gibson et al. (2007) who coupled the SRS method with the fully nonlinear Fourier-based model of Bateman et al. (2001). However, so far this has only been achieved for unidirectional seas. Therefore, as realistic sea states are directional, it is necessary to revert to the SRS with second-order wave theory and build on the work of Tromans et al. (2007).

This paper will add to the literature by employing the SRS method to investigate various bi-modal sea-states. These sea states will combine various fetch-limited wind-seas described by the JONSWAP spectrum . Some

authors have observed the occurrence of set-up below field measurements of *rogue* waves (Toffoli et al., 2007; Taylor et al., 2006). Toffoli et al. (2006) undertook time-domain simulations based on the second-order model of Sharma and Dean (1981). These simulations modelled two identical JONSWAP spectra with different mean directions of propagation. When the separation between the mean direction of propagations of the two seas was approximately 90°, a set-up was predicted by the second-order model. One of the aims of the present paper is to investigate whether a set-up is predicted by second-order theory when fetch-limited wind-seas interact with swells as often occurs in the real ocean.

This paper continues by briefly summarising the SRS method. Following this, the simulations undertaken and results obtained from the SRS will be discussed. Finally, the last section will draw the conclusions and present the wider implications of the work.

2. Spectral Surface Response Method

The application of the spectral response surface method to crest statistics is described elsewhere (Tromans and Vanderschuren, 2004). In this section, it suffices to summarise it briefly and to discuss the enhancements made to enable the description of the wind-sea and swell sea state and the isolation of the sum- and difference-terms.

A random linear sea can be represented as the sum of many frequency components, where each component obeys a Normal distribution. Using the second-order wave interactions of Sharma and Dean (1981), the non-linear surface elevation can be expressed as a function of the linear components and their Hilbert transforms. The resultant expression allows us to use a First Order Reliability Method (FORM) type of analysis, treating a constant value of ocean surface elevation as the limit state. This is a widely applicable approach, requiring only that the variable chosen to define the limit state can be expressed in terms of underlying linear wave components.

The underlying linear ocean surface elevation, $\eta^{(1)}$, is a sum of N components and can be written in the usual way as

$$\eta^{(1)} = \sum_i^N \eta_i = \sum_i^N a_i \cos\left(\mathbf{k}_i\mathbf{x} - \omega_i t + \phi_i\right), \tag{1}$$

where, for each component, a_i is the random amplitude, ω_i is frequency, ϕ_i is the random phase angle, and t is time. The values of a_i are chosen such that the first-order surface satisfies, on average, a directional bi-modal spectrum. At each step in frequency the spectrum was discretised over direction in equal energy packets.

Most of the waves in a random sea are small and obey a linear model. However, the larger waves that determine the air-gap problem exhibit higher, sharper crests associated with non-linearity. We can account for this by the second-order correction to the ocean surface given by Sharma and Dean (1981)

$$\eta^{(2)} = \eta^{(2)+} + \eta^{(2)-}, \tag{2}$$

$$\eta^{(2)+} = \frac{1}{4}\sum_i^N\sum_j^N a_i a_j K_{ij}^{+} \cos\left(\psi_i + \psi_j\right), \tag{3}$$

$$\eta^{(2)-} = \frac{1}{4}\sum_i^N\sum_j^N a_i a_j K_{ij}^{-} \cos\left(\psi_i - \psi_j\right), \tag{4}$$

where $\psi_i = \mathbf{k}_i\mathbf{x} - \omega_i t + \phi_i$, $\eta^{(2)+}$ and $\eta^{(2)-}$ are the second-order sum- and difference-terms with their corresponding kernels K^+ and K^- respectively. The contributions of $\eta^{(2)+}$ and $\eta^{(2)-}$ to the total water surface elevation are considered in this paper.

The frequency components can be transformed into standardised (unit-variance, zero mean) variables by dividing each by its standard deviation, σ,

$$x_i = \frac{\eta_i}{\sigma_i} \quad \text{and} \quad \tilde{x}_i = \frac{\tilde{\eta}_i}{\sigma_i}, \tag{5}$$

where the tilde indicates a Hilbert transform. The Hilbert transform of a variable may be thought of as the variable with all its Fourier components advanced by $\pi/2$. The joint density function of the standardised variables, $\{x_i, \tilde{x}_i\}$, is then unit-variance Normal with no correlation between the variables.

Using the expressions above, we can write the total (first- plus second-order) surface elevation as

$$\eta = \sum_{i}^{N} \sigma_i x_i + \sum_{i}^{N} \sum_{j}^{N} \{F_{ij}\sigma_i\sigma_j x_i x_j + H_{ij}\sigma_i\sigma_j \tilde{x}_i \tilde{x}_j\} \ , \tag{6}$$

Setting η to be constant in equation (6) defines a hyper-surface (of constant ocean surface elevation) in the space of $\{x_i, \tilde{x}_i\}$. We recall that $\{x_i, \tilde{x}_i\}$ have a joint Normal distribution with zero cross-correlation. Thus, surfaces of constant probability density are concentric hyper-spheres in the space of the standardised variables. The probability density is highest at the origin and falls monotonically as a function of distance from the origin. Under these circumstances, the hyper-surface defined by a constant value of η can be treated as a limit state in a FORM type of analysis. The point on the limit state hyper-surface where the distance to the origin is shortest and, therefore, the probability density greatest is the "design point" To a good approximation this is the point where a maximum in η is most likely.

The distance, β, from the origin to the design point provides an estimate of the probability, Q, of a maximum above the value η and, hence, an estimate of the statistics of crest elevation

$$Q = \exp\left(\frac{-\beta^2}{2}\right). \tag{7}$$

The inclusion of bi-modal sea is achieved by writing the combined sea state frequency-direction spectrum, $G(f, \theta)$, as the sum of the swell component and the wind-sea component

$$G(f, \theta) = G_{swell}(f, \theta) + G_{sea}(f, \theta) \tag{8}$$

In turn, the swell spectrum is written as the product of the frequency variance density spectrum, $S_{swell}(f, \theta)$, and the frequency-dependent directional distribution, $D(f, \theta)$

$$G_{swell}(f, \theta) = S_{swell}(f) D_{swell}(f, \theta), \tag{9}$$

with a similar expression for the wind-sea component. A log-normal function is used to describe the swell variance density spectrum, and a JONSWAP spectrum is used to describe the wind-sea variance density spectrum. The directional distributions of Ewans (1998) and Ewans (2001) are used to describe the directional distributions of the wind-sea and swell respectively.

3. SIMULATIONS

Several simulations were undertaken to investigate the effects of different environmental conditions with combined wind-sea and swell. The wind-seas were generated from JONSWAP spectra (Hasselmann et al., 1973) with fetch relationships developed by Carter (1982) for the Phillips parameter, α, and peak frequency, f_p. In terms of the fetch, x, and constant wind speed, u, these are given by

$$\alpha = 0.0662 X^{-0.2} \tag{10}$$

$$\tilde{f}_p = 2.84 X^{-0.3} \tag{11}$$

where $X = gx/u^2$ and $\tilde{f}_p = f_p u/g$ with g being the gravitational acceleration.

Based on these equations, five fetch-limited JONSWAP spectra were generated with different fetch lengths but a constant wind speed of $u = 20\mathrm{m/s}$. The properties of all five fetch-limited JONSWAP spectra (labelled A to E) are presented in Table 1 and plotted in Figure 1. All five wind-sea spectra were combined with a log-normal swell of $H_s = 3\mathrm{m}$, standard deviation of $\sigma = 0.015\mathrm{Hz}$ and a variety of peak periods from $5\mathrm{s}$ below to $10\mathrm{s}$ above the peak period of the wind-sea. This range of swell peak periods was chosen to investigate a variety of relative peak periods and also minimise the difference between the peak periods of the wind-sea and swell. Concerning the latter, the second-order solution of Sharma and Dean (1981) is known to produce spurious

				H_s/λ_p [-]	
Spectrum	Fetch [km]	H_s [m]	T_p [s]	Deep	Shallow
A	200	5.09	9.19	0.039	0.042
B	400	7.21	11.31	0.036	0.044
C	600	8.83	12.78	0.035	0.046
D	800	10.19	13.93	0.034	0.048
E	1000	11.40	14.89	0.033	0.049

TABLE 1. Parameters for the fetch-limited wind-sea JONSWAP spectra with a constant wind speed of $20\mathrm{m/s}$ (see Figure 1)

results when two components are widely separated. This problem is generally not of great concern if the energy contained by the two components is small, such as the interaction between the low- and high-frequency tails of the spectrum. However, when the two peaks of the bi-modal spectrum themselves are widely separated, this causes significant spurious values that produce physically unrealistic results. As such, the present simulations were chosen so as to avoid this problem.

Considering all JONSWAP spectra, the peak periods of swell vary from a minimum of $4.19\mathrm{s}$ to a maximum of $19.89\mathrm{s}$. Whilst the smaller peak periods in this range are unlikely for swell seas, they are not impossible and could be generated by short duration winds that occur some distance from the point of interest.

Every combination of wind-sea and swell was first constrained to be run as a unidirectional simulation. The directional spreading of Ewans (1998) and Ewans (2001) for the wind-sea and swell respectively was then considered. For the directional cases, the angle between the mean direction of propagation of the wind-sea and swell was also varied. Furthermore, the whole group of simulations was undertaken in deep and shallow water with depths of $d = 2000\mathrm{m}$ and $30\mathrm{m}$ respectively.

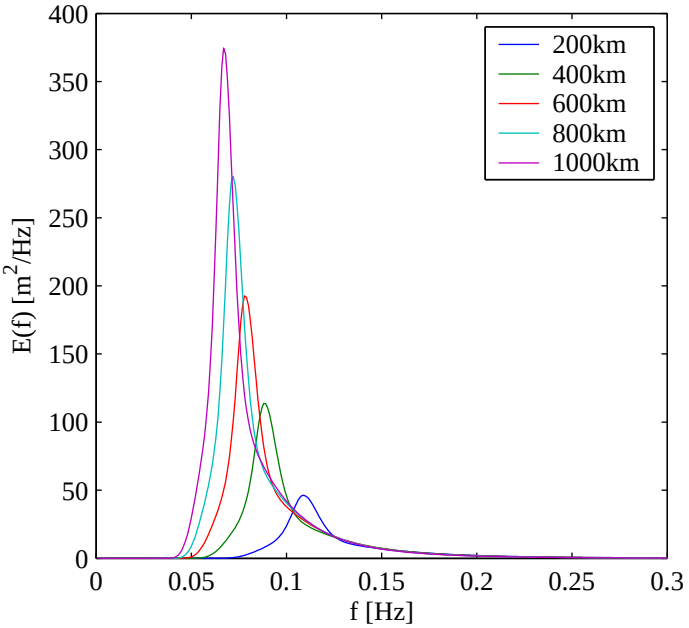

FIGURE 1. JONSWAP spectra for seas generated from different fetch lengths.

4. Discussion of Results

Considering the deep water ($d = 2000\mathrm{m}$) runs, Figures 2 and 3 present the unidirectional and directional simulations respectively. For all JONSWAP spectra these figures present the total water surface elevation (η/H_s), the second-order sum-terms ($\eta^{(2)+}/H_s$) and difference-terms ($\eta^{(2)-}/H_s$) normalised by the significant wave height. A probability of exceedance of 0.001 was chosen, representing a three-hour sea state. These contour plots demonstrate the effect of varying the relative peak period ($T_{p,swell} - T_{p,sea}$) and relative mean direction of propagation ($\Delta\theta = \theta_{swell} - \theta_{sea}$) between the wind-sea and swell.

Focusing on the deep-water, unidirectional simulations presented in Figure 2, it is clear that for all cases, as the relative peak period decreases the ratios η/H_s, $\eta^{(2)+}/H_s$ and $|\eta^{(2)-}/H_s|$ increase. This can be explained by the fact that the steepness of the swell increases as T_p, and thus λ_p, decrease. As a result, the second-order correction factors are larger. Moving down the rows of sub-plots in Figure 2 the ratios η/H_s, $\eta^{(2)+}/H_s$ and $|\eta^{(2)-}/H_s|$ decrease as the fetch, and thus the peak period, of the wind-sea increases. Once again, this can be explained as the shorter fetches produce smaller peak periods, which result in a steeper wave field (see column H_s/λ_p in Table 1), and therefore, these ratios are larger. Furthermore, a point to notice is that all the difference terms are negative, predicting a set-down beneath the extreme wave group as expected.

Moving onto the deep-water, directional simulations presented in Figure 3, for all cases, as the relative peak period decreases the ratio of η/H_s increases, once again due to the increase swell steepness. Considering the relative mean direction of propagation, the largest value of η/H_s occurs very close to the co-linear condition, and the minimum appears at approximately $\Delta\theta = 110^\circ$. As in the unidirectional cases, the steepest wind-seas produce the largest η/H_s ratios. Considering the sum- and difference-terms, their magnitude increases and decreases respectively as the relative mean direction of propagative decreases. However, as the sum-terms are approximately an order of magnitude greater than the difference-terms, the former dominate to produce the largest η/H_s ratios when $\Delta\theta$ is smallest. Moreover, unlike in the deep-water, unidirectional simulations, there are conditions in which positive difference-terms are predicted, yielding a set-up beneath the extreme wave group. Although these set-up values are small in magnitude, they are more apparent in the steeper wind-sea states when $\Delta\theta > 90^\circ$.

Figures 4 and 5 present the same contour plots as Figures 2 and 3, however, for the shallow water ($d = 30\mathrm{m}$) simulations. The shallow-water, unidirectional simulations illustrated by Figure 4 predict the same behaviour for the ratio η/H_s as discussed for the deep-water equivalent. The sum- and difference-terms, however, differ from their deep-water counterparts. In this case the location of the minimum value for each wind-sea spectrum shifts. This is due to shallow water effects becoming more significant as the peak period of both the wind-sea and the swell increase, and thus the relative water depth decreases.

Considering the shallow-water, directional simulations presented in Figure 5, the minimum value occurs at $\Delta\theta \approx 120^\circ$ and the maximum at $\Delta\theta \approx 10^\circ$. These results are consistent with Tromans et al. (2007) and the latter agrees with the findings of Forristall (2000), who plotted the second-order interaction kernel for shallow water and illustrated that its greatest value occurs just off the co-linear condition. In the shallow water cases, set-ups are also predicted for the combined conditions with the steepest wind-sea states. However, once again, the magnitude of the sum-terms is significantly greater than the difference-terms, and thus the former dominate.

5. Conclusions

This paper has concerned the extreme crest elevation occurring within a variety of combined unidirectional and directional sea-states in deep and shallow water depths. The nonlinearity of the wave field was considered up to a second-order approximation using the solution of Sharma and Dean (1981) and the probability of exceedance of a given crest elevation was calculated using the response surface method of Tromans and Vanderschuren (2004). Furthermore, the role of second-order sum- and difference-terms in generating these extremes was examined.

The following conclusions can be drawn from the present study.

(1) In both deep and shallow water, the steepest wind-seas (produced by the shortest fetch lengths) interacting with the steepest swells resulted in the largest value for the crest elevation to significant wave height ratio.
(2) For directional simulations, the largest crest elevation to significant wave height ratio occurred when the wind-sea and swell were propagating at a angle of approximately $\Delta\theta = 5^\circ$ and 10° to each other in deep and shallow water respectively.
(3) Likewise, the smallest ratio occurred at approximately $\Delta\theta = 110^\circ$ and 120° in deep and shallow water respectively.
(4) The difference-terms from the unidirectional simulations in both deep and shallow water depths always produced a set-down beneath the extreme wave group.
(5) In contrast, the directional simulations did predict set-up beneath some extreme wave groups, in particular when the steepest wind-seas combined with the steepest swells propagating at $\Delta\theta > 90^\circ$.
(6) Generally, the second-order sum-terms were significantly larger than the difference-terms (up to an order of magnitude greater in the deep-water simulations). Therefore, they dominated the behaviour of the total water surface elevation. Consequently, even when a set-up was predicted by the difference-terms, this had a negligible effect on the total crest elevation.

ACKNOWLEDGEMENT

The authors gratefully acknowledge the support of Shell International Exploration and Production.

REFERENCES

T. E. Baldock, C. Swan, and P. H. Taylor. A laboratory study of nonlinear surface waves on water. *Philosophical Transactions of the Royal Society of London A*, 354:649–676, 1996.

W. J. D. Bateman, C. Swan, and P. H. Taylor. On the efficient numerical simulation of directionally-spread surface water waves. *Journal of Computational Physics*, 174:277–305, 2001.

E. Bitner-Gregersen and Oisten Hagen. Effects of two-peak spectra on wave crest statistics. In *Proceedings of the 22nd International Conference on Offshore Mechanics and Artic Engineering, OMAE*, 2003.

D.J.T. Carter. Prediction of wave height and period for a constant wind velocity using the jonswap results. *Ocean Engineering*, 9(1):17 – 33, 1982. ISSN 0029-8018.

M. A. Donelan and A. K. Magnusson. The role of meteorological focusing in generating rogue wave conditions. In *Proceedings of Aha Hulikoa Hawaiian Winter Workshop, University of Hawaii at Manoa.*, 2005.

K. C. Ewans. Directional spreading in ocean swell. In *Proceedings of the 4th International Symposium Waves*, 2001.

K. C. Ewans. Observations of the directional spectrum of fetch-limited waves. *Journal of Physical Oceanography*, 28(3):495–512, 1998.

G.Z. Forristall. Wave crest distributions: Observations and second order theory. *Journal of Physical Oceanography.*, 30:1931–1943, 2000.

R. Gibson and C. Swan. The evolution of large ocean waves: the role of local and rapid spectral changes. *Philosophical Transactions of the Royal Society of London A.*, 463:21–48, 2007. doi: 10.1098/rspa.2006.1729.

R. S. Gibson, C. Swan, and P. S. Tromans. Fully nonlinear statistics of wave crest elevation calculated using a Spectral Response Surface method: Application to unidirectional sea states. *Journal of Physical Oceanography*, 37:3–15, 2007.

K. Hasselmann, T. P. Barnet, E. Bouws, H. Carlson, D. E Cartwright, K. Enke, K. Ewing, J. A. Ewing, H. Gienpp, D. E. Hasselmann, P. Kruseman, A. Meerburg, P. Müller, D. J. Olbes, K. Richter, K. Sell, and H. Walden. *Measurments of Wind-Wave Growth and Swell Decay during the Joint North Sea Wave Project (JONSWAP)*. Deutsches Hydrographisches Institut, 1973.

S. Haver and O. J. Anderson. Freak waves — rare realizations of a typical population or typical realzations of a rare population? In *Proceedings of 10th ISOPE Conference.*, 2000.

J. N. Sharma and R. G. Dean. Second-order directional seas and associated wave forces. *Society of Petroleum Engineering Journal*, 4:129–140, 1981.

P. H. Taylor, T. A. A. Adcock, A. G. L. Borthwick, D. A. G. Walker, and Y. Yao. The nature of the Draupner giant wave of 1st January 1995 and the assocaited sea-state, and how to estimate directional spreading from an Eulerian surface elevation time history. In *Proceedings of the 9th International Workshop on Wave Hindasting and Forecasting*, 2006.

A. Toffoli, M. Onorato, and J. Monbaliu. Wave statistics in unimodal and bimodal seas from a second-order model. *European Journal of Mechanics B - Fluids*, 25(5):649–661, 2006.

A. Toffoli, M. Onorato, A. V. Babanin, E. Bitner-Gregersen, A. R. Osborne, and J. Monbaliu. Second-order theory and setup in surface gravity waves: A comparison with experimental data. *Journal of Physical Oceanography*, 37(11):2726–2739, 2007.

P. Tromans and L. Vanderschuren. A Spectral Response Surface method for calculating crest elevation statistics. *Journal of Offshore Mechanics and Arctic Engineering*, 126:51–53, 2004.

P. Tromans, L. Vanderschuren, and K. C. Ewans. Second order statistics of high waves in wind sea and swell. In *Proceedings of the 26th International Conference on Offshore Mechanics and Artic Engineering, OMAE*, 2007.

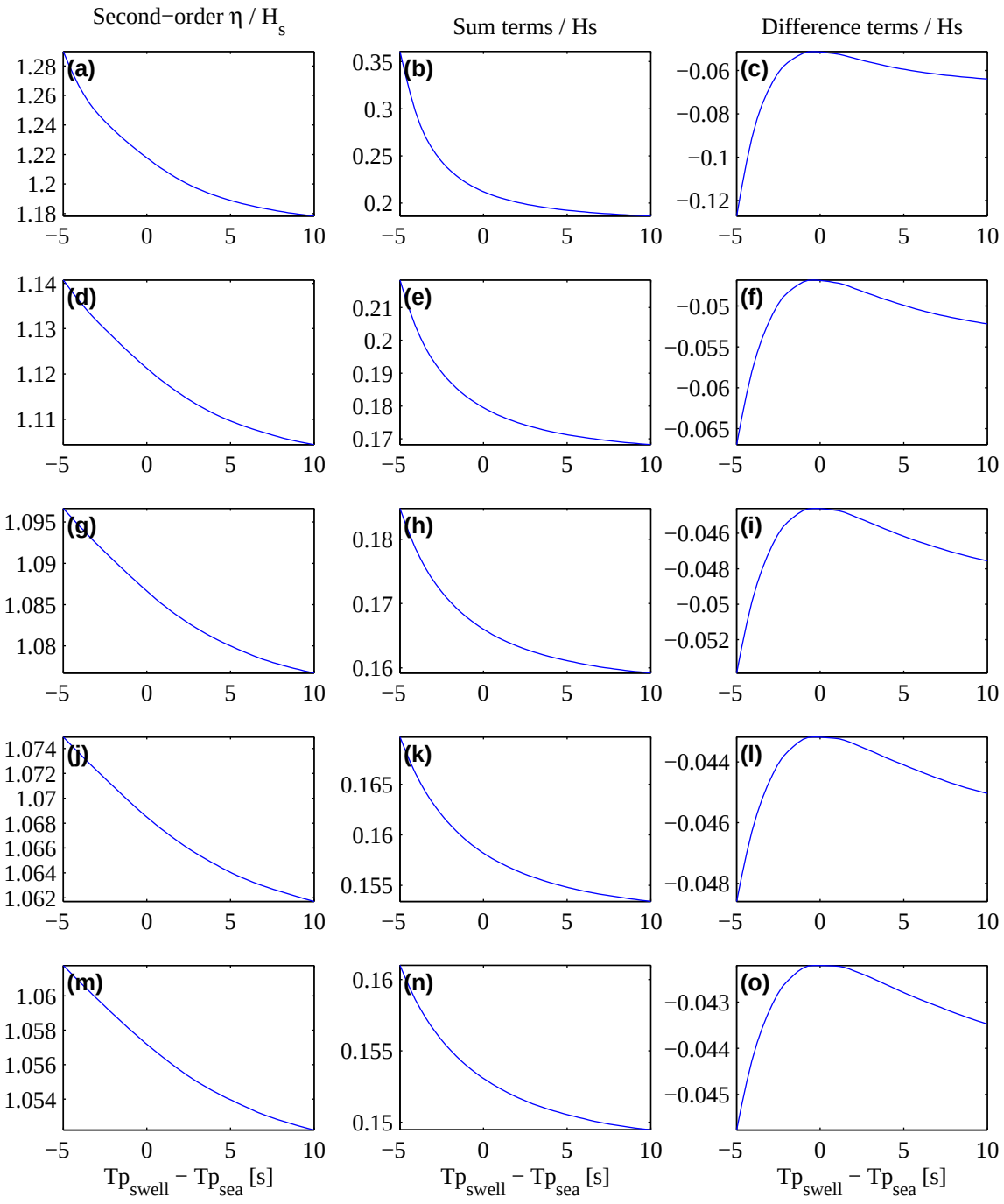

FIGURE 2. Unidirectional, deep-water simulations ($d = 2000\mathrm{m}$). (a), (b) and (c) JONSWAP spectra A; (d), (e) and (f) JONSWAP spectra B; (g), (h) and (i) JONSWAP spectra C; (j), (k) and (l) JONSWAP spectra D; (m), (n) and (o) JONSWAP spectra E. All combined with a swell of $H_s = 3\mathrm{m}$ and $\sigma = 0.015\mathrm{Hz}$.

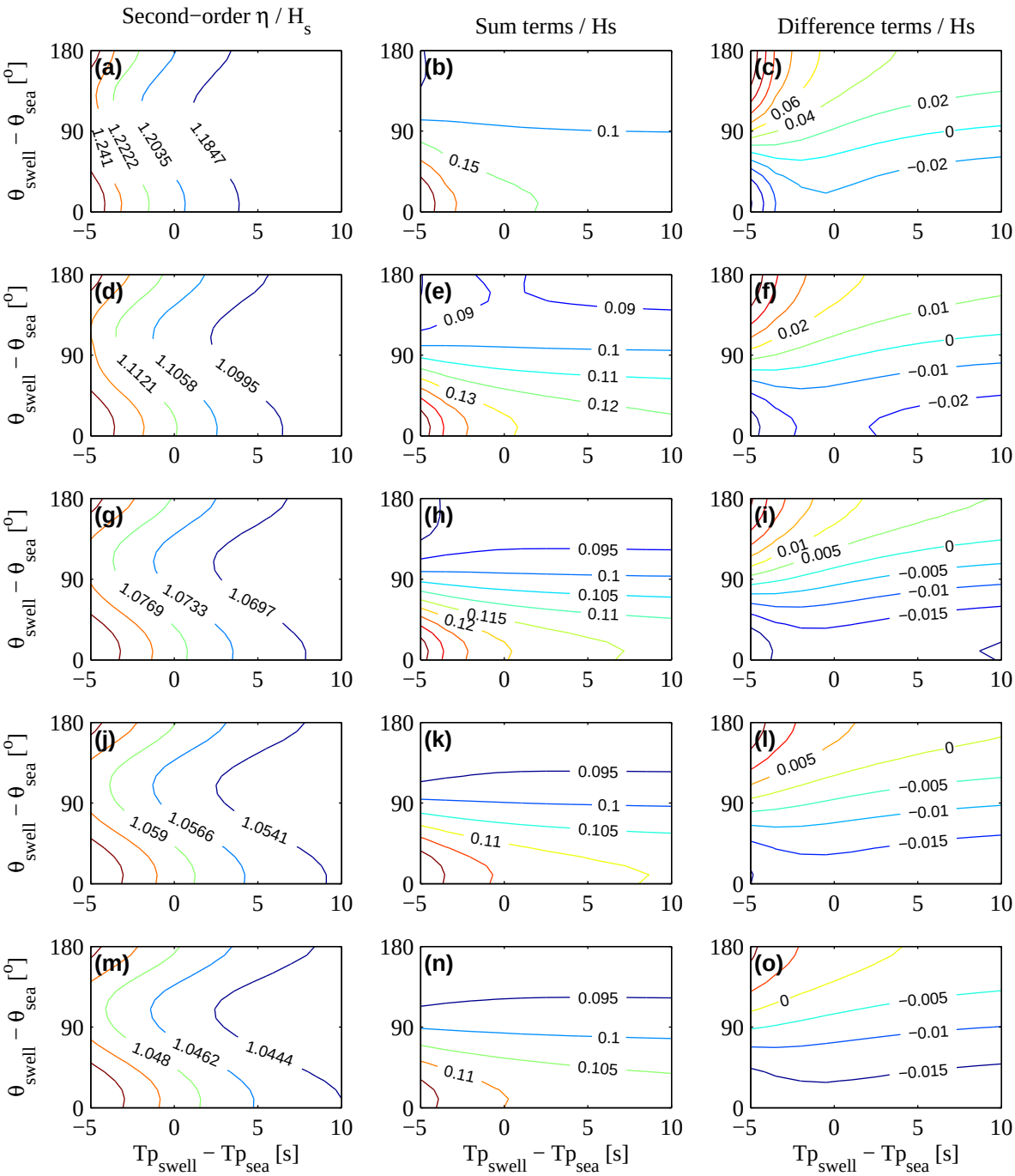

FIGURE 3. Directional, deep-water simulations ($d = 2000\text{m}$). (a), (b) and (c) JONSWAP spectra A; (d), (e) and (f) JONSWAP spectra B; (g), (h) and (i) JONSWAP spectra C; (j), (k) and (l) JONSWAP spectra D; (m), (n) and (o) JONSWAP spectra E. All combined with a swell of $H_s = 3\text{m}$ and $\sigma = 0.015\text{Hz}$.

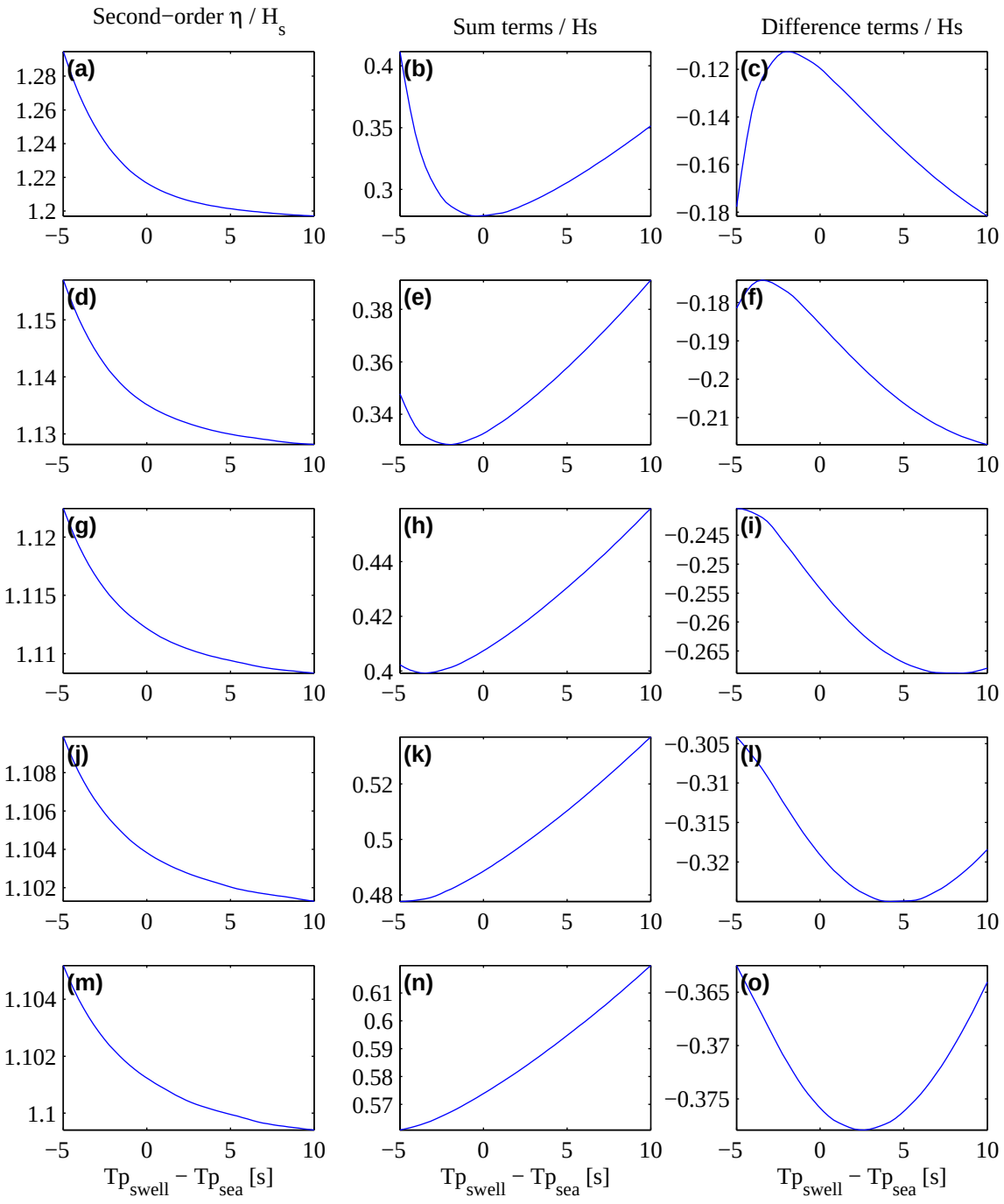

FIGURE 4. Unidirectional, shallow-water simulations ($d = 30\mathrm{m}$). (a), (b) and (c) JONSWAP spectra A; (d), (e) and (f) JONSWAP spectra B; (g), (h) and (i) JONSWAP spectra C; (j), (k) and (l) JONSWAP spectra D; (m), (n) and (o) JONSWAP spectra E. All combined with a swell of $H_s = 3\mathrm{m}$ and $\sigma = 0.015\mathrm{Hz}$.

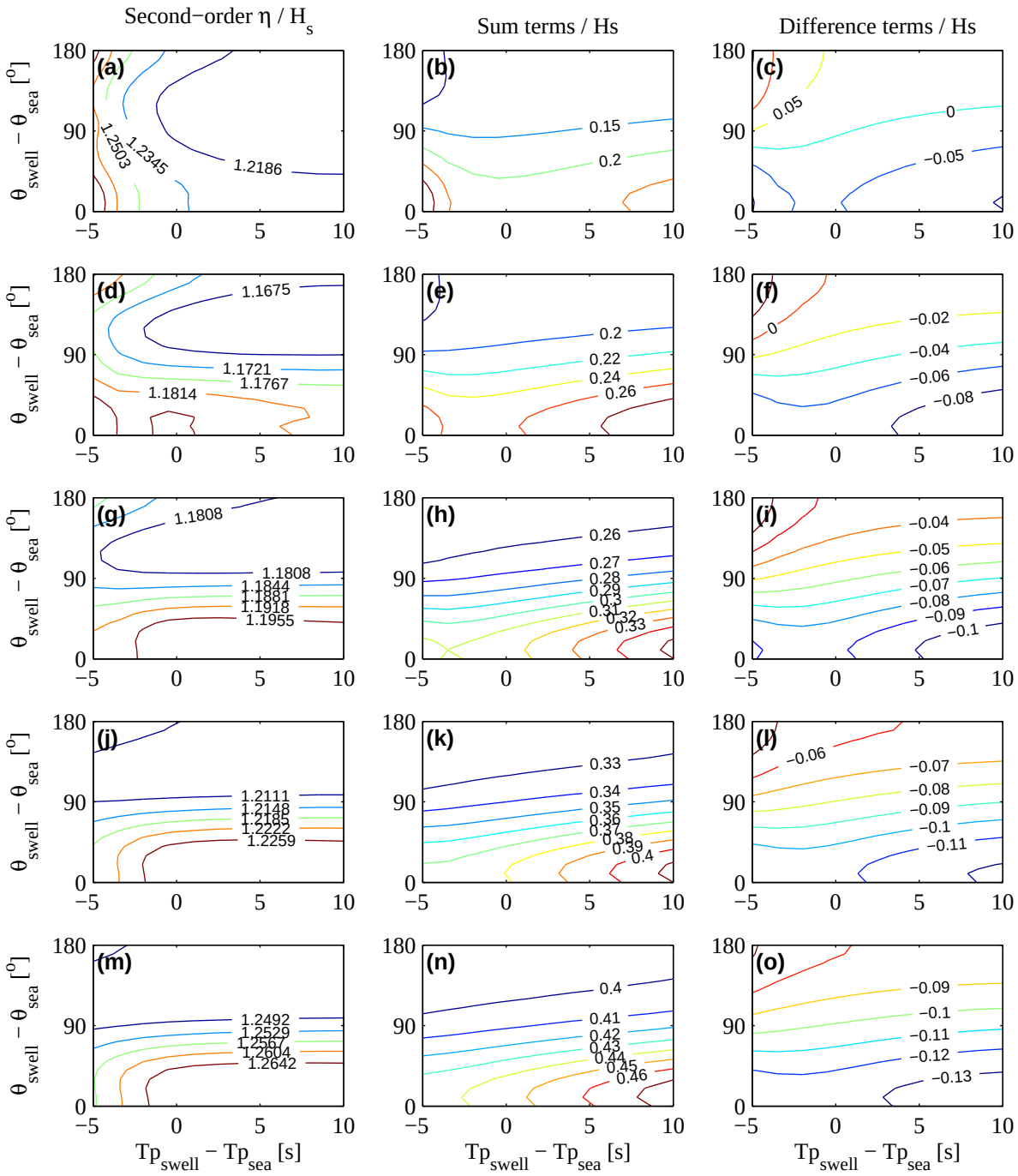

FIGURE 5. Directional, shallow-water simulations ($d = 30\text{m}$). (a), (b) and (c) JONSWAP spectra A; (d), (e) and (f) JONSWAP spectra B; (g), (h) and (i) JONSWAP spectra C; (j), (k) and (l) JONSWAP spectra D; (m), (n) and (o) JONSWAP spectra E. All combined with a swell of $H_s = 3\text{m}$ and $\sigma = 0.015\text{Hz}$.